Photoinduced magnetization effect in a *p*-type $Hg_{1-x}Mn_xTe$ single crystal investigated by infrared photoluminescence

Liangqing Zhu,[1,2,*] Jun Shao,[2,†] Xiren Chen,[2] Yanqiu Li,[1] Liang Zhu,[2] Zhen Qi,[2] Tie Lin,[2] Wei Bai,[1] Xiaodong Tang,[1] and Junhao Chu[1,2]

[1]*Key Laboratory of Polar Materials and Devices, Ministry of Education, East China Normal University, Shanghai 200062, China*

[2]*National Laboratory for Infrared Physics, Shanghai Institute of Technical Physics, Chinese Academy of Sciences, Shanghai 200083, China*

(Received 29 October 2015; revised manuscript received 7 August 2016; published 5 October 2016)

Photoinduced magnetization (PIM) effect of $Hg_{1-x}Mn_xTe$ provides an attractive solution for realizing the quantum anomalous Hall effect in quantum wells with a light field. In this paper, the PIM effect of *p*-type $Hg_{0.74}Mn_{0.26}Te$ single crystal was investigated by power-, polarization- and temperature-dependent photoluminescence (PL) measurements in both reflection and transmission geometries. Giant Zeeman splitting and polarization of PL spectra were observed without an external magnetic field evolving with excitation-power density of the pumping laser and temperature, which were accounted for by the PIM effect. The occurrence of the PIM was qualitatively understandable by the carrier-mediated mean-field theory known as the *Zener model*. The results indicate that infrared PL measurements with enhanced sensitivity and signal-to-noise ratio can serve as a convenient pathway for clarifying the PIM effect of semimagnetic semiconductors.

DOI: 10.1103/PhysRevB.94.155201

I. INTRODUCTION

The manipulation of the magnetization of magnetic systems without resorting to external magnetic fields is attractive for spintronics and memory storage devices [1,2]. In semimagnetic or diluted magnetic semiconductors (SMSCs or DMSs), the strong spin-spin interactions between band electrons and localized magnetic ions lead to a host of entirely new magneto-optical physical phenomena, such as giant Faraday, giant Kerr, photoinduced magnetization (PIM) effects, among which only the PIM effect can regulate spins without external magnetic field. The PIM effect was first demonstrated in $Hg_{1-x}Mn_xTe$ by Krenn *et al.* using a detecting method of combining circularly polarized optical pumping with a superconducting quantum-interference device (SQUID) [3,4]. Later on, a number of experiments on the PIM effect were reported in SMSCs or DMSs systems of, e.g., $Cd_{1-x}Mn_xTe$ [5–7], (Ga,Mn)As thin films [8,9], and (In,Mn)As/GaSb heterostructure [10,11], and theoretical studies predicted the PIM effect in $Hg_{1-x}Mn_xTe$ to be an attractive solution using a light field to generate a magnetic field and realizing the quantum anomalous Hall (QAH) effect in quantum wells [12–14]. The mechanism of the PIM effect in $Hg_{1-x}Mn_xTe$ was hence an interesting, crucial, but unfortunately not well-understood problem.

Besides the macroscopic features of magnetization, Zeeman splitting of conduction and valence bands can serve as another important fingerprint for the PIM effect, which can be directly detected from spectral information. While a SQUID-based technique is an easy and sensitive way of measuring the strength of macroscopic magnetization, it falls short of measuring the Zeeman splitting and the spin polarization of carriers induced by photoinduced magnetic field and is thus difficult for in-depth understanding of the PIM effects in SMSCs or DMSs. Photoluminescence (PL) as a nondestructive optical spectroscopy is convenient and efficient for clarifying the electronic band structures, impurity levels, and carriers spin polarization of semiconductors [15–17]. In narrow-gap SMSCs, however, shallow impurities may act as a serious disturbance in recognizing the Zeeman splitting of band-to-band/free exciton (FX) recombination, possibly causing the application of PL for the PIM effect to be blank to date.

In this paper we perform power-, polarization-, and temperature-dependent infrared PL measurements on a *p*-type $Hg_{1-x}Mn_xTe$ single crystal, with improved sensitivity and signal-to-noise ratio [18,19] and concurrent reflection and transmission collection geometries to eliminate the PL component relative to shallow impurities [20]. Simultaneously, the power- and temperature-dependent PL characteristics of a nonmagnetic *p*-type $Hg_{1-x}Cd_xTe$ single crystal are also studied for the express purpose of excluding the possibility of the PIM effect from nonmagnetic factors. Without external magnetic field, giant Zeeman splitting and polarization of a *p*-type $Hg_{1-x}Mn_xTe$ single crystal are identified to evolve with excitation power density, which is well accounted for by the PIM effect and consistent qualitatively with the prediction of the carrier-mediated mean-field theory. For a quantitative understanding of the mechanism of the PIM effect in a *p*-type $Hg_{1-x}Mn_xTe$ single crystal, however, the contribution of local magnetization of bound magnetic polaron (BMP) complexes should be considered.

II. EXPERIMENTAL DETAILS

A *p*-type $Hg_{0.74}Mn_{0.26}Te$ single crystal prepared by the modified Bridgeman method and annealed in Hg vapor was used, with an acceptor concentration N_A of about 4.7×10^{16} cm^{-3} measured by Hall experiments and a thickness d of about 300 μm [21]. Furthermore, two comparative samples were also measured to exclude nonmagnetic factors in this paper. One was a *p*-type $Hg_{0.627}Cd_{0.373}Te$ film ($d \approx 10$ μm) grown on CdZnTe by liquid phase epitaxy (LPE) for the purpose of excluding the laser heating effect, and the

*lqzhu@ee.ecnu.edu.cn
†jshao@mail.sitp.ac.cn

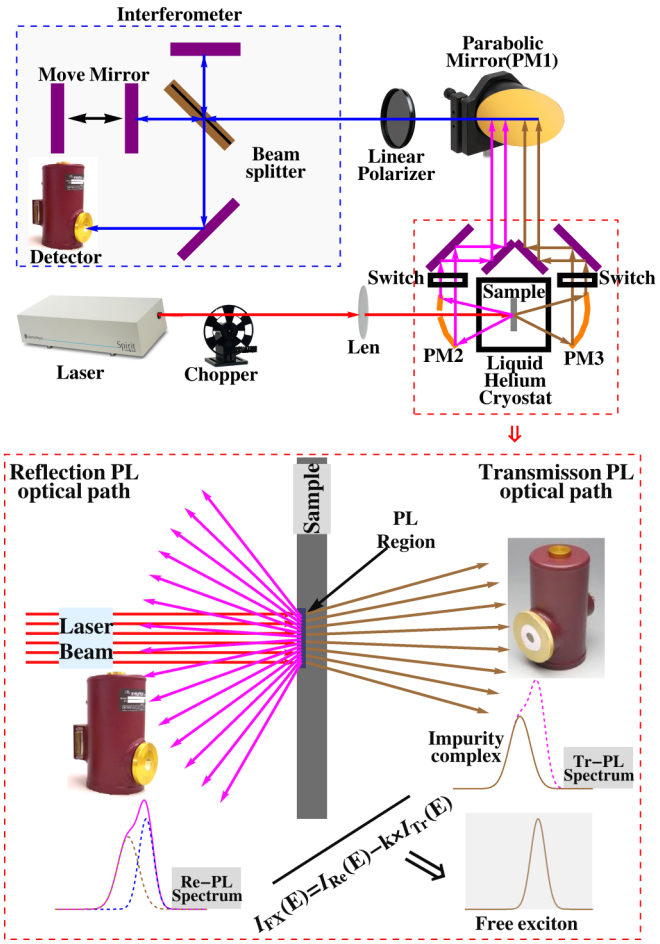

FIG. 1. Schematic map of the concurrent detection PL method. The upper shows the main optical paths and the lower illustrates the way that derives the PL spectrum of band-to-band/FX recombination.

other was a weak p-type $Hg_{0.8}Mn_{0.2}Te$ single crystal ($N_A \approx 2.0\times10^{15}$ cm^{-3} and $d \approx 300$ μm) annealed in Hg vapor two times to exclude the band-gap renormalization effect.

PL measurements were conducted with a step-scan Fourier transform infrared (FTIR) spectrometer-based modulated PL method [16,19] in concurrent reflection and transmission PL-signal collection geometries. A combination of liquid-nitrogen cooled InSb detector and KBr beamsplitter was configured for a sensitive spectral range of about $0.3 \sim 0.8$ eV. The spectral resolution was 6 cm^{-1}. The sample's temperature was controlled by a liquid helium cryostat. The excitation source was a 647 nm Kr^+ cw laser whose spot diameter and actual excitation power on the sample surface was about 100 μm and between 0.8–125 mW, respectively. The output laser was linearly polarized. For polarization-dependent PL measurements, a wire-grid (WG) polarizer was placed at the entrance of the spectrometer for gauging the polarization degree of the PL spectrum.

Figure 1 sketches the main optical paths and working principle of the concurrent detection PL method, in which the upper part shows the main optical paths and the lower part illustrates the way that derives the PL spectrum of band-to-band/FX recombination, $I_{FX}(E)$, from the reflection PL (Re-PL) and transmission PL (Tr-PL) spectra. The Re-PL and Tr-PL spectra are measured by switching two switches under the same experimental conditions. The intensity of Re-PL, $I_{Re}(E)$, was proportional to the intensity of Tr-PL, $I_{Tr}(E)$, because of different signal collection efficiencies. The proportional coefficient k was, however, a constant. Due to the self-absorption above the band gap being much stronger than that below the band gap in the Tr-PL, the PL of band-to-band/FX recombination $I_{FX}(E)$ can hence be derived with

$$I_{FX}(E) = I_{Re}(E) - kI_{Tr}(E). \quad (1)$$

III. RESULTS AND DISCUSSION

A. The photoluminescence evidence of photoinduced magnetization effect

Figure 2(a) shows the power-dependent (1–160 W/cm^2) PL spectra of the p-type $Hg_{0.74}Mn_{0.26}Te$ sample at $T = 5$ K without external magnetic field ($B = 0$ T). Magnifications are made to normalize the PL intensities. The Re-PL spectra are depicted in black solid lines, whose shape changes significantly as the excitation power density (P) rises. The Tr-PL spectra are plotted in magenta dashes, which are multiplied by a coefficient $k = 0.72$.

The Tr-PL signal was proven to be from a neutral acceptor-BMP bound exciton [(A^0,X)BMP] transition [20]. The peak energy $E_{(A^0,X)BMP}$, as shown in Fig. 2(b), first increases with P and then decreases as P gets higher than a critical value of about $P_c^{BMP} \simeq 20$ W/cm^2. The corresponding photocarrier density is estimated to be about 1×10^{16} cm^{-3}. The change of $E_{(A^0,X)BMP}, \Delta E^{RS}_{(A^0,X)BMP}$ is 2.3 meV when P rises from P_c^{BMP} to 160 W/cm^2. Meanwhile, the full width at half maximum (FWHM) gets broader with P as depicted in Fig. 2(c).

Figure 2(d) illustrates the PL spectra of FX calculated from those in Fig. 2(a) by Eq. (1). As indicated by two long arrows, the high- and low-energy edges show a blue- and redshift, respectively, simultaneously as P rises, which may hint at a *peak-splitting* process. The energy and FWHM of the FX PL peak are plotted in Figs. 2(e) and 2(f), respectively, against excitation power density. The E_{FX} first blueshifts and then redshifts as P rises, with the turning point at critical excitation power density P_c^{FX} of about 20 W/cm^2, nearly identical to the P_c^{BMP} seen in Fig. 2(a). The redshift of $E_{FX}, \Delta E^{RS}_{FX}$ is about 5.4 meV when P rises from P_c^{FX} to 160 W/cm^2. A ratio of $\Delta E^{RS}_{(A^0,X)BMP}/\Delta E^{RS}_{FX}$ is hence derived to be 0.43 for the power density range from 20 to 160 W/cm^2. The FWHM manifests a surging and declining with a turning point at P_c^{FX} and gets broader steadily as P goes beyond P_c^{FX}.

Figure 3 shows the results of power-dependent concurrent PL spectra of p-type $Hg_{0.74}Mn_{0.26}Te$ at $T = 10$ K. It can be found that the power-dependent behavior of (A^0,X)BMP and FX at 10 K are similar to that of (A^0,X)BMP and FX at 5 K. As depicted in Figs. 3(a) and 3(c), the $E_{(A^0,X)BMP}$ and the E_{FX} also first increase with P and then decrease as P gets higher than a critical value, however, both the P_c^{BMP} and the P_c^{FX} are about 40 W/cm^2 which is greater than that of about 20 W/cm^2 at 5 K. The $\Delta E^{RS}_{(A^0,X)BMP}$ and the ΔE^{RS}_{FX} are about 1.2 meV and 2.4 meV at 10 K, respectively, when P rises from the critical value to 160 W/cm^2. So the ratio of $\Delta E^{RS}_{(A^0,X)BMP}/\Delta E^{RS}_{FX}$ is

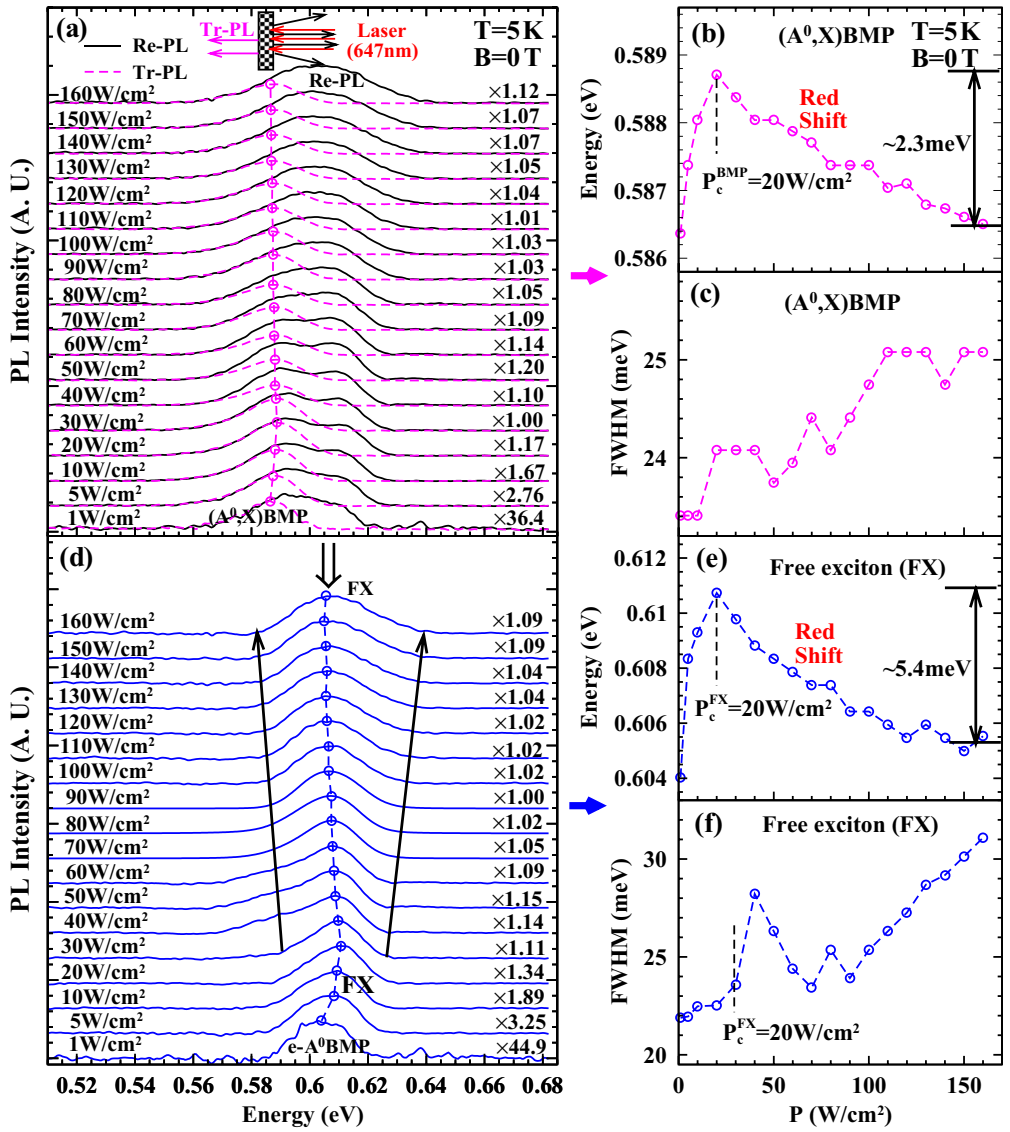

FIG. 2. PL spectra of p-type $Hg_{0.74}Mn_{0.26}Te$ in reflection (Re-PL) and transmission (Tr-PL) geometries at $T = 5$ K under different excitation. (a) Re-PL spectra in black solid lines and Tr-PL in magenta dashes; (b) energy and (c) FWHM of (A^0,X)BMP's PL versus excitation power density; (d) deduced PL spectra of FX; (e) energy and (f) FWHM of the FX's PL.

about 0.5 at 10 K, close to 0.43 at 5 K. These experimental observations prompt the possibility that the energy redshift of and the FWHM broadening of the (A^0,X)BMP and FX PL features are both due to the PIM-induced giant Zeeman splitting.

To make a verification, we first look qualitatively at the band diagram of Zeeman splitting. Figure 4(a) shows the schematic of the energy levels and optical transitions in p-type zinc blende SMSCs with and without macroscopic magnetization ($\langle M\rangle = 0$ and $\langle M\rangle \neq 0$). For $\langle M\rangle = 0$, the Γ_6 conduction band (CB), Γ_8 valence band (VB), and the acceptor level remain twofold, fourfold, and fourfold degenerate, from which band exciton and (A^0,X)BMP PL transitions may be observed as illustrated in Fig. 4(b). For $\langle M\rangle \neq 0$, the band degeneracies are lifted and in total six transitions are possible with four observable in the Faraday configuration; this may be due to the hole localization caused by magnetic polaron effect at low temperature and lead to weak spin relaxation in the valence band of p-type $Hg_{1-x}Mn_xTe$ [21]. As the PL spectrum approaches its quasi-steady-state shape as defined by the distribution of electrons and holes, the Zeeman splitting of the CB and VB will lead to the redshift and broadening rather than resolvable PL features, as sketched in Fig. 4(b).

We then calculate quantitatively the redshifts of the E_{FX} and $E_{(A^0,X)BMP}$ due to the PIM effect using the modified Pidgeon-Brown model [22]. The giant Zeeman splitting of the heavy-hole type FX can be described as

$$\Delta E_{FX}(B) = N_0(|\alpha| + |\beta|)x_{eff}\, SB_S\left[\frac{g\mu_B\, SB}{k_B(T + T_{AF})}\right], \quad (2)$$

where B is *magnetic field*. $N_0\alpha$ and $N_0\beta$ are the exchange constants of the CB and VB and take the values of 0.4 eV and -0.6 eV, respectively, in HgMnTe [23]. $S = 5/2$ and $g = 2$ are the spin and g-factor of Mn^{2+} ions. B_S is the Brillouin function of the spin S. x_{eff} is the effective Mn component. T_{AF} is the temperature related to the antiferromagnetic Mn-Mn

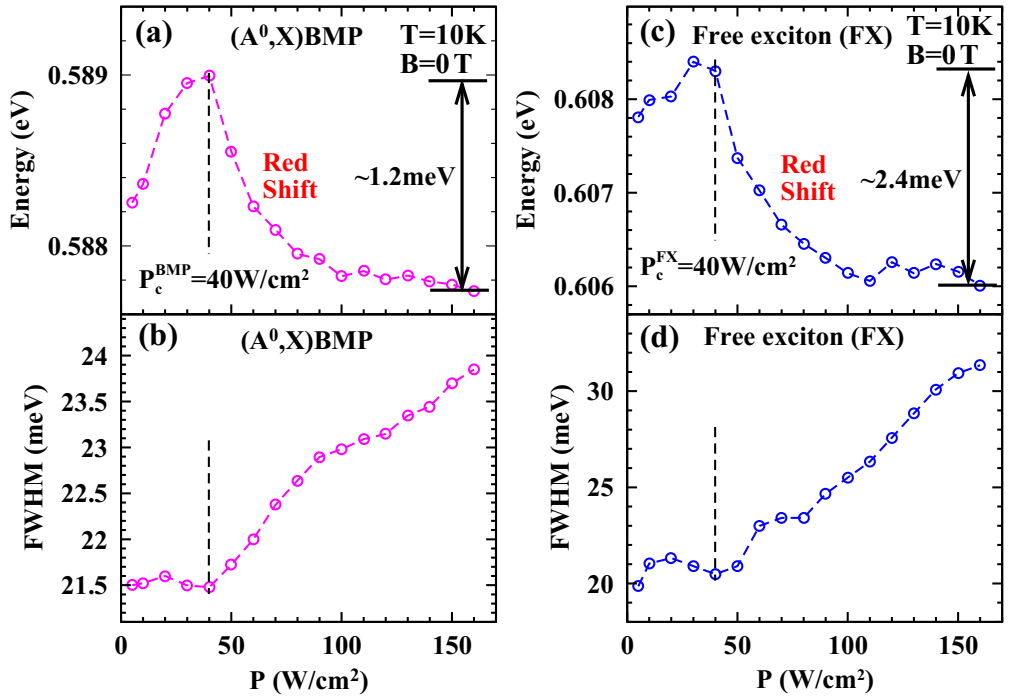

FIG. 3. The results of power-dependent concurrent PL spectra of p-type $Hg_{0.74}Mn_{0.26}Te$ at $T = 10$ K. (a) Energy and (b) FWHM of (A^0,X)BMP's PL versus excitation power density; (c) energy and (d) FWHM of the FX's PL.

exchange interaction. The (A^0,X)BMP can be described in analogy to a neutral donor of A^0X ground state in nonmagnetic semiconductor [24,25], as the ground-state wave function is approximately asymmetric for the two internally paired strongly localized holes and one externally unpaired extended electron spin. The exchange interaction between the unpaired electron and the Mn^{2+} ions contributes to the variation of polaron energy of (A^0,X)BMP, and the giant Zeeman splitting of (A^0,X)BMP is directly related to that of the FX [22],

$$\Delta E_{(A^0,X)\mathrm{BMP}}(B) = \frac{|N_0\alpha|}{|N_0\alpha| + |N_0\beta|}\Delta E_{\mathrm{FX}}(B)\,. \qquad (3)$$

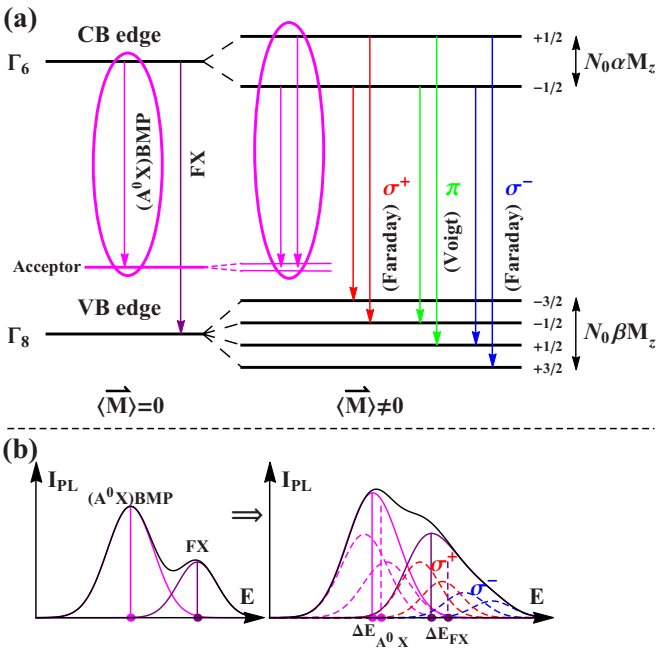

FIG. 4. (a) Energy levels and optical transitions of p-type zinc-blende SMSCs without magnetization ($\langle M\rangle = 0$) and with macroscopic magnetization ($\langle M\rangle \neq 0$). (b) Schematic of PL spectrum from the $\langle M\rangle = 0$ to $\langle M\rangle \neq 0$ ignoring the spin relaxation of the valence band.

The ratio $\Delta E_{(A^0,X)\mathrm{BMP}}/\Delta E_{\mathrm{FX}}$ is deduced by Eqs. (2) and (3) to be 0.4, very close to the ratio $\Delta E^{\mathrm{RS}}_{(A^0,X)\mathrm{BMP}}/\Delta E^{\mathrm{RS}}_{\mathrm{FX}}$ of 0.43 at 5 K and of 0.5 at 10 K as derived by the PL analysis. This indicates that the redshift of the PL spectra with power density can be described quantitatively with the PIM effect-induced giant Zeeman splitting.

Further verification of the PIM can be made through polarization-dependent PL measurements in the Re-PL and Tr-PL geometries. The representative polarization PL spectra are shown in Fig. 5 for the p-type $Hg_{0.74}Mn_{0.26}Te$ sample at 5 K and 10 K without an external magnetic field.

At low excitation power density, the intensity and shape of Re-PL and Tr-PL spectra passing through the polarizer do not change obviously with the rotation of the polarizer, e.g., 0°,45°, and 90°, as shown in Figs. 5(a), 5(d), and 5(h). At high excitation power density, however, the intensity and shape change obviously with the rotation, as shown in Figs. 5(c), 5(f), and 5(j). According to Malus' law for a polarizer, the polarization state of the sample's PL is circular polarized light at low excitation power density or partial polarized light at high excitation power density.

To have a quantitative description of the polarization evolution with excitation power density, the definition of

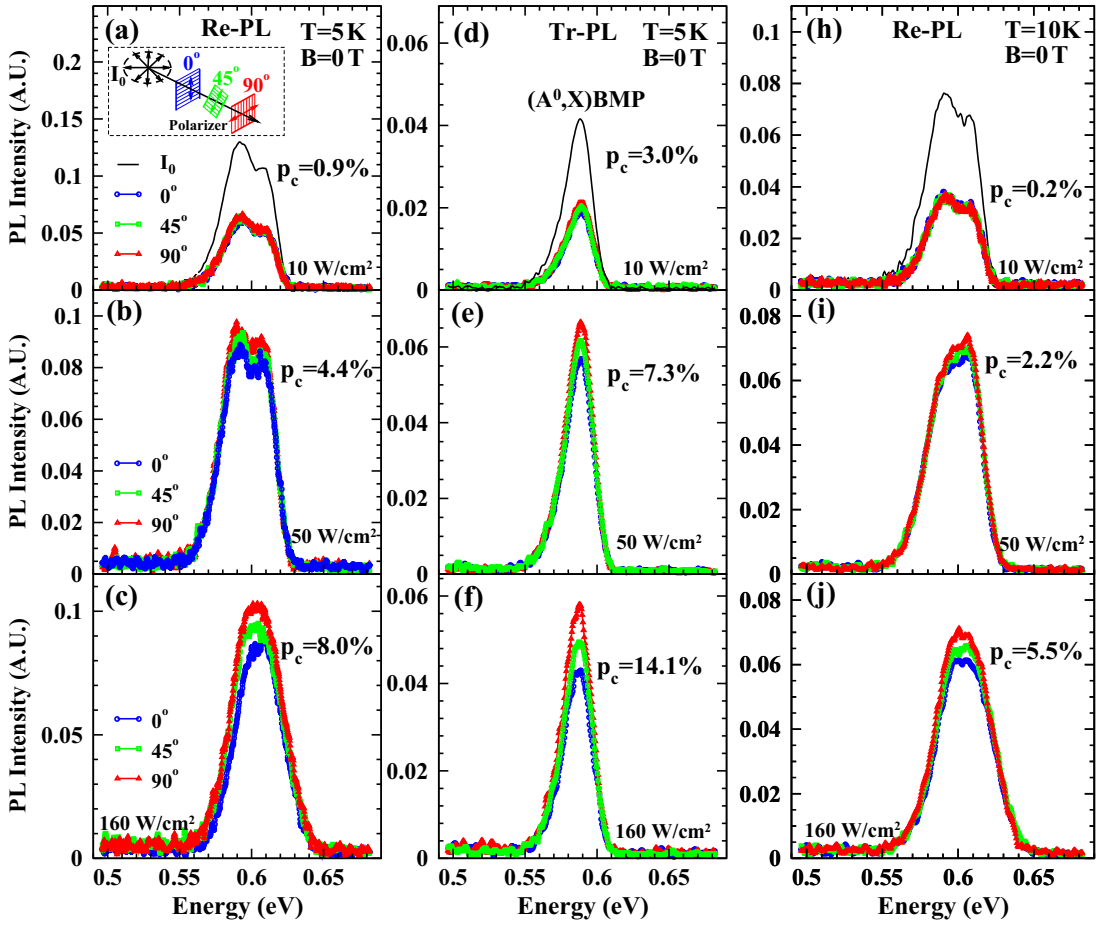

FIG. 5. The polarization degree evaluation of power-dependent PL of the p-type $Hg_{0.74}Mn_{0.26}Te$ sample at 5 K and 10 K. (a)–(c) for Re-PL at 5 K, (d)–(f) for Tr-PL at 5 K, and (h)–(j) for Re-PL at 10 K, respectively. p_c for circular polarization degree.

circular polarization degree is employed as

$$p_c = \frac{I_{max} - I_{min}}{I_{max} + I_{min}} \times 100\%, \quad (4)$$

which represents the polarization induced by a magnetic field in the Faraday geometry [22]. I_{min} and I_{max} are PL intensities detected in 0° and 90° polarizations [relative to the direction of the WG polarizer at the minimum I, as sketched in the inset of Fig. 5(a)], respectively. At $T = 5$ K, it is clear that the p_c of p-type $Hg_{0.74}Mn_{0.26}Te$ sample increases with excitation power density for both the Re-PL and the Tr-PL: It increases from 0.9% to 8.0% for the Re-PL and from 3.0% to 14.1% for the Tr-PL when the power density rises from 10 to 160 W/cm^2. Moreover the p_c also changes with temperature. Figures 5(h)–5(j) show the polarization degree of Re-PL spectrum evolution with the excitation power density at 10 K. At the same excitation power density, the p_c of 10 K is less than that of 5 K. This provides further support for the existence of PIM effect in the p-type $Hg_{0.74}Mn_{0.26}Te$ and the weak spin relaxation in the valence band.

B. Exclusion of laser heating effect

In order to eliminate the possibility that the laser heating effect leads to the energy redshift of the (A^0,X)BMP and FX in power-dependent PL spectra, temperature-dependent Re-PL and Tr-PL spectra of p-type $Hg_{0.74}Mn_{0.26}Te$ were also measured at $P = 1$ W/cm^2 from 2 K to 77 (60) K, as shown in Fig. 6. It can be found that (1) the lineshape of Re-PL and Tr-PL spectra doesn't change with temperature, in clear contrast to the peak splitting in the power-dependent PL measurements; (2) the Re-PL peak energy versus temperature shows first a blueshift from 2 to about 25 K, but then a slight redshift from about 25 to 77 K. The redshift value of Re-PL spectra is about 1.4 meV as temperature rises to 77 K, which is far less than that of (A^0,X)BMP (about 2.3 meV) and of FX (about 5.4 meV) mentioned in power-dependent PL. (3) The peak FWHM of Re-PL spectra gets narrower from 2 K to about 25 K, which is also different from that of power-dependent PL measurements. (4) More importantly the peak energy evolution of temperature-dependent Tr-PL is opposite to that of power-dependent Tr-PL [Fig. 2(b)].

In addition, as a comparative study, we check power- and temperature-dependent PL of a p-type $Hg_{0.623}Cd_{0.373}Te$ sample under similar experimental conditions as those for the p-type $Hg_{0.74}Mn_{0.26}Te$ sample. Figures 7(a) and 7(b) illustrate the typical power-dependent PL spectra and energy evolution curve of the p-type $Hg_{0.623}Cd_{0.373}Te$ at 5 K. Figures 7(c) and 7(d) show the typical temperature-dependent PL spectra and energy evolution curve of the p-type $Hg_{0.623}Cd_{0.373}Te$ under excitation power of $P_{ex} = 20$ W/cm^2.

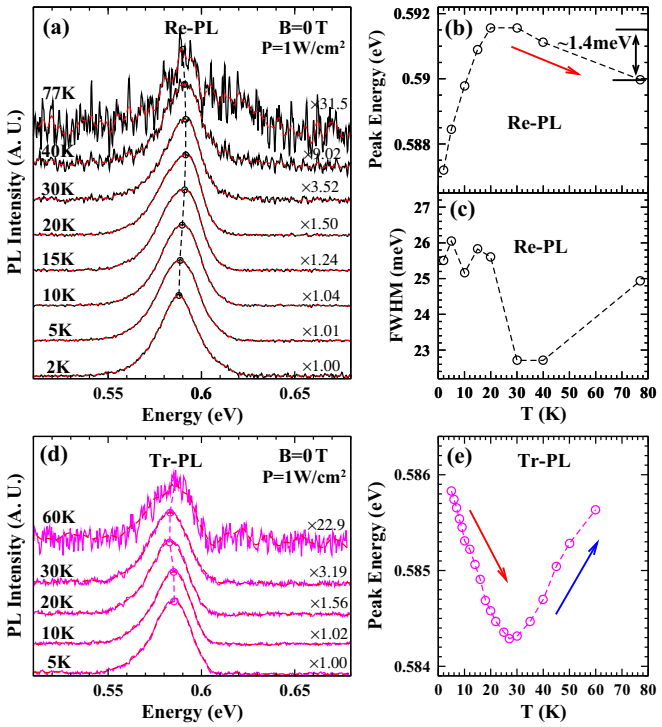

FIG. 6. The evaluation of temperature-dependent PL of the p-type $Hg_{0.74}Mn_{0.26}Te$ sample in reflection (a)–(c) and transmission (d), (e) geometries at 1 W/cm^2.

Comparing Figs. 7(a) and 7(b) and Figs. 7(c) and 7(d), it is clear that (i) the band gap of p-type $Hg_{0.623}Cd_{0.373}Te$ increases with excitation power density (P), and the blueshift is about 0.6 meV and 2.0 meV, when P gets enhanced from 10 W/cm^2 to 160 and 350 W/cm^2, respectively, and (ii) the band gap increases with temperature, and the blueshift is about 50 meV when temperature rises up from 5 to 290 K. If we assume the blueshift in the power-dependent measurement to be solely due to laser heating effect, the maximum temperature increment $\Delta T_{\max}$ would be $\leqslant$ 5 K when P_{ex} gets to 160 W/cm^2.

Then if similarity is considered between the $Hg_{0.623}Cd_{0.373}Te$ and $Hg_{0.74}Mn_{0.26}Te$ samples in the power-dependent PL experiments under similar experimental conditions, the maximum temperature increment of these samples should be $\leqslant$5 K. Therefore these results can exclude the laser heating effect in the analysis of the redshift of (A^0,X)BMP and FX in the power-dependent PL measurements by the concurrent Re/Tr-PL method.

C. Exclusion of band-gap renormalization effect

The band-gap renormalization (BGR) effect due to significant carrier density is to be expected when the density is of the order of the exciton volume, i.e., $n_c \sim a_B^{-3}$ (Mott criterion), where a_B is the Bohr radius of the exciton [26,27]. The BGR effect can lead to a decrease of the optical absorption edge or the band gap E_g. In order to eliminate the possibility that BGR effect leads to the energy redshift of the (A^0,X)BMP and FX in power-dependent PL spectra, we analyze from the following two aspects.

On one hand, the critical exciton concentration n_c of BGR effect is estimated by Mott criterion in the p-type $Hg_{0.74}Mn_{0.26}Te$ sample. For $Hg_{1-x}Mn_xTe$ single crystal, the static dielectric constant $\epsilon_s = 20.5 - 32.6x + 25.1x^2$, the electron effective mass $m_e^*/m_e = 5.7\times10^{-16}(\text{eV cm}^2)E_g/P^2$ where the unit of E_g is eV, the hole effective mass $m_h^* = 0.45m_e$, and the Kane momentum matrix element $P = (-8x + 8.35)\times10^{-8}$ eV cm [4,28,29]. Then the exciton reduced mass $\mu \sim 0.07m_e$ and $a_B \sim 10.39$ nm in the p-type $Hg_{0.74}Mn_{0.26}Te$ sample, so the n_c of BGR effect is about 1.12×10^{18} cm^{-3}.

However this value is an order of magnitude larger than the number of photons that are absorbed by the p-type $Hg_{0.74}Mn_{0.26}Te$ sample during the lifetime τ of exciton (about ns to μs level in direct band-gap semiconductors). For a simple estimate of the exciton concentration upper limit for power-dependent PL experiments, we assume (i) the reflectivity of the sample R is $\sim$0.2625 ($R = [(n-1)/(n+1)]^2, n = \sqrt{\epsilon_\infty}$ and $\epsilon_\infty = 15.2 - 28.8x + 28.2x^2$) [28], (ii) one photon ($h\nu$) absorbed by the sample generates one exciton, (iii) $\tau = 0.1\,\mu$s refers to typical minority carrier radiative lifetime in p-type HgCdTe [30,31], and (iv) laser penetration depth l_m is about 10 μm, then the maximum exciton concentration is

$$n_{e,h}^{\max} = \frac{P(1-R)\tau}{h\nu l_m} \sim 3.0\times10^{16}\ \text{cm}^{-3}.$$

On the other hand, according to the material properties of $Hg_{1-x}Mn_xTe$ single crystal, the lower the Mn component, the smaller the effective mass of the electron. The BGR effect is more likely to occur in the sample with lower Mn component. Therefore a comparative experiment about the power-dependent PL spectra of the weak p-type $Hg_{0.8}Mn_{0.2}Te$ sample was conducted under the same conditions, as shown in Fig. 8. It can be found that (i) the intensity of Tr-PL is much weaker than that of Re-PL, implying a very low concentration of acceptor; (ii) the peak energy of both (A^0,X)BMP (Tr-PL) and FX (Re-PL) show blueshift with increasing P, which proves that there is no BGR effect in the weak p-type $Hg_{0.8}Mn_{0.2}Te$ sample. Hence the BGR effect does not exist in the p-type $Hg_{0.74}Mn_{0.26}Te$ sample when $P < 160$ W/cm^2. In fact, as widely reported in the literature [26], band-gap renormalization as a many-body effect is usually observed in low-dimensional structure with extremely high excitation power density at a level above 10^5 W/cm^2, which is far beyond what we could achieve in our study.

D. Photoinduced magnetization mechanism of p-type $Hg_{1-x}Mn_xTe$

To understand well the mechanism of the PIM effect, previous studies established valuable models. For example, Krenn *et al.* thought of the origin as the circularly polarized light-induced orientation of the Mn ions in the effective field of spin-polarized electrons [4], and Mishra *et al.* described theoretically a Hamiltonian model of localized magnetic moments interacting with photoexcited itinerant carriers [32]. In general, the magnetization mechanism based on a carrier-mediated mean-field (MF) theory can be qualitatively in agreement with the itinerant carriers-induced magnetization

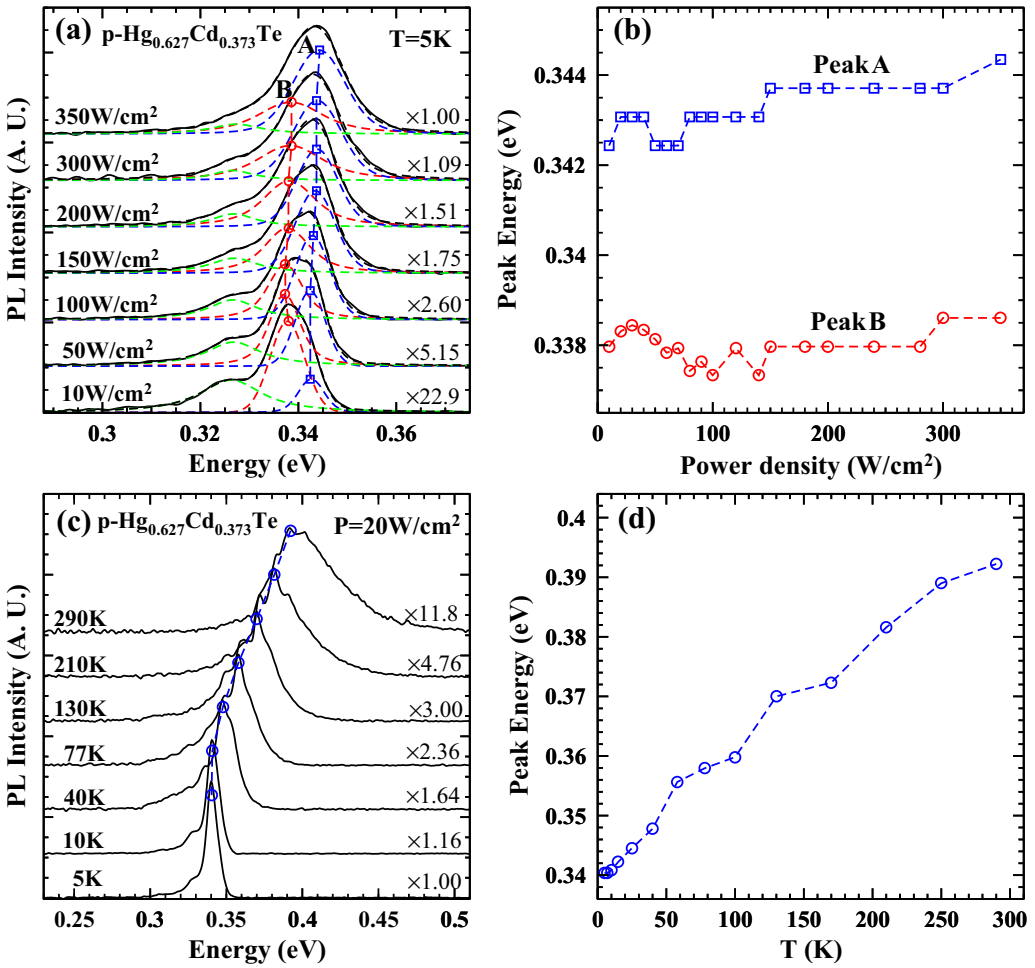

FIG. 7. (a) and (b) are the typical power-dependent (10–350 W/cm^2) PL spectra and PL energy evolution curves of p-type $Hg_{0.623}Cd_{0.373}Te$ at 5 K. (c) and (d) are the typical temperature-dependent (5–290 K) PL spectra and the PL energy evolution curve of p-type $Hg_{0.623}Cd_{0.373}Te$ at $P_{ex} = 20$ W/cm^2.

(M) in, e.g., (Ga,Mn)As [33,34]. In particular, the *Zener model* considers M as a solution of the mean-field equation by minimizing the Ginzburg-Landau free-energy function [35],

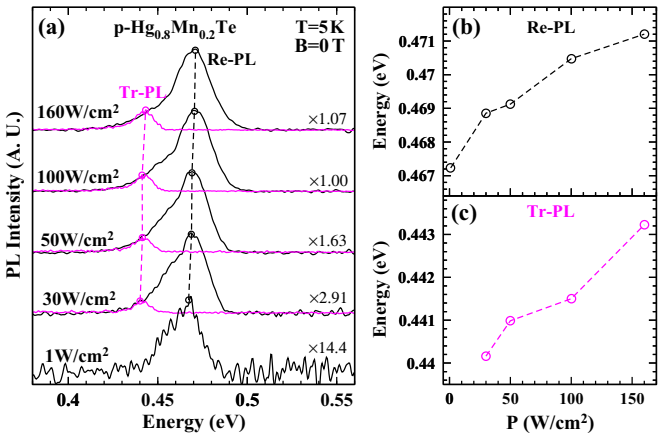

FIG. 8. Power-dependent PL spectra of the weak p-type $Hg_{0.8}Mn_{0.2}Te$ sample in reflection (Re-PL) and transmission (Tr-PL) geometries at $T = 5$ K (a), the peak energy of Re-PL (b), and the peak energy of Tr-PL (c).

$F[M] = F_c[M] + F_S[M]$, and

$$M = N_0 x_{\text{eff}}\, g\mu_B S B_S\left[\frac{g\mu_B S\,(-\partial F_c[M]/\partial M + B)}{k_B\,(T + T_{\text{AF}})}\right], \quad (5)$$

where $F_c[M]$ and $F_S[M]$ are the free-energy functions of carriers and localized spins, respectively. T is temperature, B is magnetic field, and n_c is carrier concentration. At the beginning of the PIM when M is small, $F_c[M]$ can be expressed according to Landau's phenomenological theory of the second-order phase transition as [34,36]

$$F_c[M] = F_c[0] - \frac{A_F \rho_s(T)\beta^2}{2(2\,g\mu_B)^2} M^2 + \alpha_4 M^4\,, \quad (6)$$

where A_F and α_4 are parameters of greater than zero, and $\rho_s(T)$ is the spin density of states. For nondegenerate carriers, $\rho_s(T) = n_c(T)$, but for a strongly degenerate carriers liquid, $\rho_s(T) = m^*\sqrt[3]{3n_c(T)/\pi^4}/\hbar^2$ in three dimensions, and m^* is the carrier effective mass. By expanding $B_S(M)$, we arrive at

$$M = \frac{1}{2\,g\mu_B\sqrt{\alpha_4}}\sqrt{\frac{1}{4}A_F\rho_s(T)\beta^2 - \frac{3k_B\,(T + T_{\text{AF}})}{N_0 x_{\text{eff}} S(S+1)}}\,. \quad (7)$$

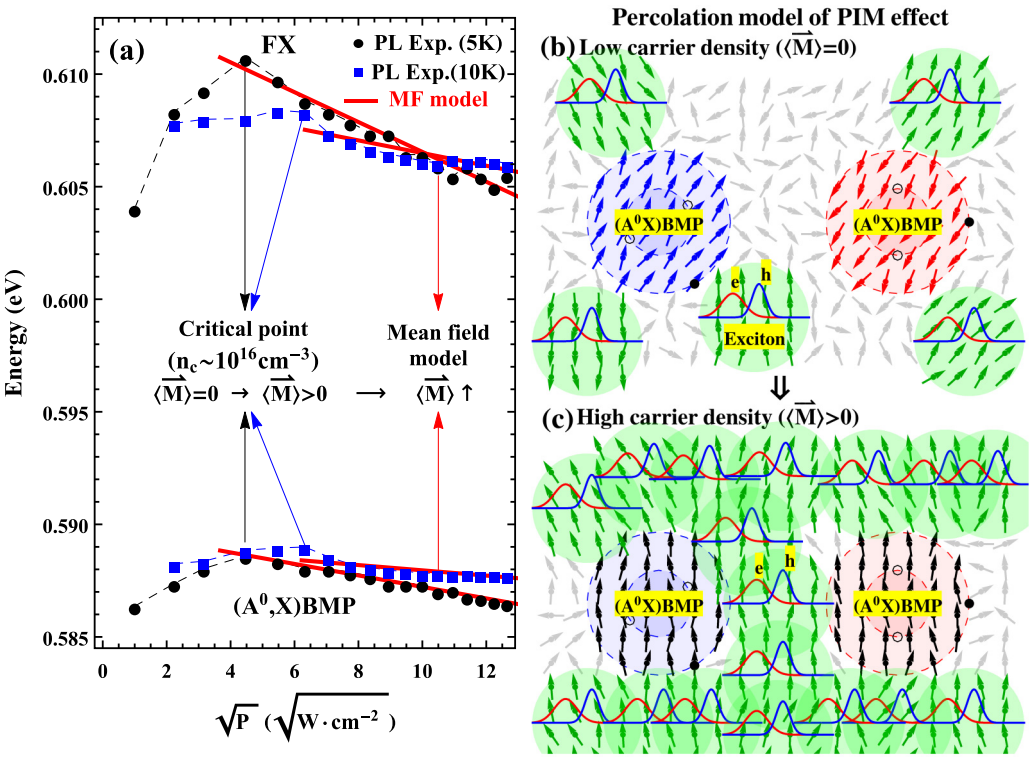

FIG. 9. (a) Comparison of power-dependent PL and the mean-field (MF) model. (b) and (c) sketch the percolation mechanism of PIM effect caused by (A^0, X)BMP complexes.

Thence we apply the *Zener model* in analyzing the PIM effect in p-type $Hg_{0.74}Mn_{0.26}Te$. At a given T, two important features can be seen from Eq. (7) that (i) the occurrence of the PIM effect ($M > 0$) demands $\rho_s(T)$ or $n_c(T)$ to be higher than a critical value of ρ_{s0} or n_{c0}, and (ii) as ρ_s or n_c increases but does not reach a degenerate concentration, the magnetization meets approximately

$$M \propto \sqrt{\rho_s(T) - \rho_{s0}} \propto \sqrt{n_c(T) - n_{c0}} \sim \sqrt{n_c} \propto \sqrt{P}\,,$$

and thus $\Delta E_{\mathrm{FX}}^{\mathrm{RS}} \propto \sqrt{P}$ and $\Delta E_{(A^0,X)\mathrm{BMP}}^{\mathrm{RS}} \propto \sqrt{P}$. Theses features are qualitatively consistent with the characteristics of the PIM effect observed in the above power-dependent PL experiments. The derived n_c is about 10^{16} cm^{-3} for the p-type $Hg_{0.74}Mn_{0.26}Te$ when $T \leqslant 10$ K, and the $\Delta E_{\mathrm{FX}}^{\mathrm{RS}}$ and the $\Delta E_{(A^0,X)\mathrm{BMP}}^{\mathrm{RS}}$ vary basically linearly with $\sqrt{P}$, as depicted in Fig. 9(a). These results indicate the PIM effect of p-type $Hg_{1-x}Mn_xTe$ to be mainly due to the carrier-mediated mean-field mechanism.

For the critical carrier concentration of $\sim 10^{16}$ cm^{-3} in the p-type $Hg_{0.74}Mn_{0.26}Te$ derived by the PL analysis being much lower than the prediction of $\sim 5\times 10^{18}$ cm^{-3} by the *Zener model*, a major reason is considered to be the fact that the *Zener model* did not consider the contribution of the local magnetization of BMP complexes like A^0BMP and (A^0,X)BMP. In fact, just as in the p-type $Hg_{0.74}Mn_{0.26}Te$, SMSCs or DMSs usually contain defects/impurities which form BMP complexes at low temperatures, especially under photoirradiation. The BMP complexes not only possess large orbit sizes from a few nm to several 10 nm, but also manifest a strong local magnetization of about several Tesla as microferromagnetic "domains" [20,21]. For a low carrier density as depicted in Fig. 9(b), the magnetization direction of the BMP complexes is random, and they do not interact with each other; the average magnetization $\langle \boldsymbol{M} \rangle$ is thus zero. As the carrier density rises as depicted in Fig. 9(c), the spatial overlap of the wave functions of carriers and BMP complexes gets stronger, causing the wave functions of adjacent BMP complexes to interconnect. The magnetization directions of each pair of adjacent BMP complexes interrelate and tend to be parallel on the basis of a magnetic percolation transition of BMP complexes [37], leading to $\langle M \rangle > 0$.

IV. SUMMARY

To conclude, the PIM effect in p-type $Hg_{0.74}Mn_{0.26}Te$ single crystal was observed experimentally by a concurrent analysis of Re-PL and Tr-PL measurements without an external magnetic field at 5 K and 10 K. Giant Zeeman splitting and polarization of the PL spectra were observed to evolve with excitation power density and temperature, which were well correlated to the PIM effect and might hint at a feasible solution of achieving QAH effect in $Hg_{1-x}Mn_xTe$ quantum well with light. The PIM effect in p-type $Hg_{1-x}Mn_xTe$ was interpretable qualitatively rather than quantitatively by the carrier-mediated mean-field theory, as the latter did not consider the contribution of local magnetization of BMP complexes. The infrared modulated PL method was shown to be effective and convenient in investigating the PIM effect optically.

ACKNOWLEDGMENTS

L.Q.Z. thanks Wanqi Jie and Tao Wang at Northwestern Polytechnical University (China) for the HgMnTe samples. The work was sponsored by the Ministry of Science and Technology 973 Program (2013CB922301 and 2014CB643901), the Shanghai Committee of Science and Technology (14YF1404100 and 13ZR1453700), the RFDP (01405286), and the National Natural Science Foundation (61604056, 61176075, and 61306119) of China.

[1] C. H. Lambert, S. Mangin, B. S. Varaprasad, Y. K. Takahashi, M. Hehn, M. Cinchetti, G. Malinowski, K. Hono, Y. Fainman, M. Aeschlimann, and E. E. Fullerton, Science **345**, 1337 (2014).
[2] A. Kirilyuk, A. V. Kimel, and T. Rasing, Rep. Prog. Phys. **76**, 026501 (2013).
[3] H. Krenn, W. Zawadzki, and G. Bauer, Phys. Rev. Lett. **55**, 1510 (1985).
[4] H. Krenn, K. Kaltenegger, T. Dietl, J. Spałek, and G. Bauer, Phys. Rev. B **39**, 10918 (1989).
[5] B. König, I. A. Merkulov, D. R. Yakovlev, W. Ossau, S. M. Ryabchenko, M. Kutrowski, T. Wojtowicz, G. Karczewski, and J. Kossut, Phys. Rev. B **61**, 16870 (2000).
[6] C. Buss, R. Pankoke, P. Leisching, J. Cibert, R. Frey, and C. Flytzanis, Phys. Rev. Lett. **78**, 4123 (1997).
[7] D. D. Awschalom, J. Warnock, and S. von Molnár, Phys. Rev. Lett. **58**, 812 (1987).
[8] Y. Hashimoto and H. Munekata, Appl. Phys. Lett. **93**, 202506 (2008).
[9] E. Rozkotová, P. Němec, P. Horodyská, D. Sprinzl, F. Trojánek, P. Malý, V. Novák, K. Olejník, M. Cukr, and T. Jungwirth, Appl. Phys. Lett. **92**, 122507 (2008).
[10] S. Koshihara, A. Oiwa, M. Hirasawa, S. Katsumoto, Y. Iye, C. Urano, H. Takagi, and H. Munekata, Phys. Rev. Lett. **78**, 4617 (1997).
[11] R. R. Subkhangulov, H. Munekata, Th. Rasing, and A. V. Kimel, Phys. Rev. B **89**, 060402(R) (2014).
[12] C. X. Liu, X. L. Qi, X. Dai, Z. Fang, and S. C. Zhang, Phys. Rev. Lett. **101**, 146802 (2008).
[13] W. Beugeling, C. X. Liu, E. G. Novik, L. W. Molenkamp, and C. Morais Smith, Phys. Rev. B **85**, 195304 (2012).
[14] X. Liu, H. C. Hsu, and C. X. Liu, Phys. Rev. Lett. **111**, 086802 (2013).
[15] J. Shao, X. Lü, S. L. Guo, W. Lu, L. Chen, Y. F. Wei, J. R. Yang, L. He, and J. H. Chu, Phys. Rev. B **80**, 155125 (2009).
[16] J. Shao, L. Chen, W. Lu, X. Lü, L. Q. Zhu, S. L. Guo, L. He, and J. H. Chu, Appl. Phys. Lett. **96**, 121915 (2010).
[17] X. R. Chen, Y. X. Song, L. Zhu, S. M. Wang, W. Lu, S. L. Guo, and J. Shao, J. Appl. Phys. **113**, 153505 (2013).
[18] J. Shao, F. Y. Yue, X. Lü, W. Lu, W. Huang, Z. F. Li, S. L. Guo, and J. H. Chu, Appl. Phys. Lett. **89**, 182121 (2006).
[19] J. Shao, W. Lu, X. Lü, F. Y. Yue, Z. F. Li, S. L. Guo, and J. H. Chu, Rev. Sci. Instrum. **77**, 063104 (2006).
[20] L. Q. Zhu, J. Shao, L. Zhu, X. R. Chen, Z. Qi, T. Lin, W. Bai, X. D. Tang, and J. H. Chu, J. Appl. Phys. **118**, 045707 (2015).
[21] L. Q. Zhu, J. Shao, T. Lin, X. Lü, J. Y. Zhu, X. D. Tang, and J. H. Chu, J. Appl. Phys. **111**, 083502 (2012).
[22] J. Kossut and J. A. Gaj, in *Introduction to the Physics of Diluted Magnetic Semiconductors* (Springer, Warsaw, 2010), pp. 232–259.
[23] E. G. Novik, A. Pfeuffer-Jeschke, T. Jungwirth, V. Latussek, C. R. Becker, G. Landwehr, H. Buhmann, and L. W. Molenkamp, Phys. Rev. B **72**, 035321 (2005).
[24] D. S. Pan, D. L. Smith, and T. C. McGill, Solid State Commun. **18**, 1557 (1976).
[25] M. Suffczynski and L. Wolniewicz, Phys. Rev. B **40**, 6250 (1989).
[26] C. F. Klingshirn, in *Semiconductor Optics,* 3rd ed. (Springer, Hong Kong, 2007), pp. 467–528.
[27] P. Vashishta and R. K. Kalia, Phys. Rev. B **25**, 6492 (1982).
[28] A. Rogalski, Infrared Phys. **31**, 117 (1991).
[29] R. Blachnik, J. Chu, R. R. Galazka, J. Geurts, J. Gutowski, B. Hönerlage, D. Hofmann, J. Kossut, R. Lévy, P. Michler, U. Neukirch, T. Story, A. Strauch, and D. Waag, in *Semiconductors: II-VI and I-VII Compounds; Semimagnetic Compounds*, edited by U. Rössler, Vol. III/41B of Landolt-Börnstein (Springer, Berlin, 1999), p. 1438.
[30] M. A. Kinch, F. Aqariden, D. Chandra, P.-K. Liao, H. F. Schaake, and H. D. Shih, J. Electron. Mater. **34**, 880 (2005).
[31] V. C. Lopes, A. J. Syllaios, and M. C. Chen, Semicond. Sci. Technol. **8**, 824 (1993).
[32] S. Mishra, G. S. Tripathi, and S. Satpathy, Phys. Rev. B **77**, 125216 (2008).
[33] T. Dietl, A. Haury, and Y. Merle d'Aubigné, Phys. Rev. B **55**, R3347(R) (1997).
[34] T. Dietl, H. Ohno, and F. Matsukura, Phys. Rev. B **63**, 195205 (2001).
[35] C. Zener, Phys. Rev. **81**, 440 (1951).
[36] R. K. Pathria, in *Statistical Mechanics*, 2nd ed. (Elsevier, Singapore, 1997), pp. 341–344.
[37] A. Kaminski and S. Das Sarma, Phys. Rev. Lett. **88**, 247202 (2002).